HST HIGH-RESOLUTION IMAGES AND MAPS OF PLUTO

S. A. STERN

Southwest Research Institute, 1050 Walnut, Street No. 426, Boulder, Colorado 80302
Electronic mail: alan@everest.space.swri.edu

M. W. BUIE

Lowell Observatory, 1400 W. Mars Hill Road, Flagstaff, Arizona 86001
Electronic mail: buie@lowell.edu

L. M. TRAFTON

McDonald Observatory, University of Texas, Austin, Texas 78712
Electronic mail: lmt@astro.as.utexas.edu

Received 1996 May 28; revised 1996 November 12

ABSTRACT

We have obtained *Hubble Space Telescope* (*HST*) images of Pluto at 410 and 278 nm which resolve numerous distinct albedo provinces on this planet. Our images were obtained using the Faint Object Camera (FOC) of the *Hubble Space Telescope* between 1994 June 20 and July 01. This dataset is the first longitudinally-complete, rotationally-resolved direct image dataset on Pluto. We have combined the various images that *HST* obtained to make maps of the planet. These images reveal that Pluto has (i) a highly variegated surface, (ii) extensive, bright, asymmetric polar regions, (iii) large midlatitude and equatorial spots, and (iv) possible linear features hundreds of kilometers in extent. The dynamic range of albedo features across the planet detected at the FOC's resolution in both the 410 and 278 nm bandpasses exceeds 5:1. We also present and discuss the multiplicative product of the *HST* 410 and 278 nm maps, which allow us to infer the location of where the cleanest, and therefore the presumably freshest ice deposits, lie. Toward the end of this report, we make some initial comparisons between the *HST*-derived maps and previously published Pluto maps derived from the inversion of ground-based light curves of Pluto. Although more sophisticated *HST* map inversions are planned, the data products presented here provide important inputs to modelers interested in volatile transport, and comparative studies of Pluto and Triton. [S0004-6256(97)03002-1]

1. INTRODUCTION

Pluto was discovered in early 1930 by Clyde Tombaugh, after a long search for the strong perturber of Uranus and Neptune, which we now know never existed (cf. Tombaugh & Moore 1980; Hoyt 1980; Standish 1996). Unfortunately, the originator of that search, Percival Lowell, did not live to enjoy Pluto's discovery.

It is fair to say that after the determination of Pluto's orbit in the early 1930s, no other important information was developed about the planet until the early 1950s. However, between 1953 and 1976, technological advances made possible several basic but important findings. Among these were the determination of Pluto's ~6.3872 day rotation period (Walker & Hardie 1955), the detection of Pluto's intrinsically red color (Fix *et al.* 1970), the discovery of Pluto's high axial obliquity (Andersson & Fix 1973), and the numerical detection of Pluto's 3:2 orbital resonance with Neptune (Cohen & Hubbard 1965; Williams & Benson 1971).

Beginning in 1976, the pace of key discoveries about Pluto increased dramatically. Among the discoveries made in rapid succession were: the discovery of methane on Pluto's surface (Cruikshank *et al.* 1976); the detection of Pluto's satellite Charon (Christy & Harrington 1978, 1980); and the prediction (Andersson 1978), detection (Binzel *et al.* 1985), and study of the once-every-124 year mutual eclipse event season (cf. Binzel 1989 for a good review). Later in the 1980s there was also the 1988 occultation of a bright star by Pluto, confirming the presence of an atmosphere (e.g., Elliot *et al.* 1989), and the 1989 Voyager 2 Neptune system encounter, which gave us important, detailed insights into Pluto's closest analog in the Solar System (e.g., Smith *et al.* 1989), Triton. In the early 1990s came detection of N_2 and CO ice on Pluto's surface (Owen *et al.* 1993). Reviews of these and other details about the Pluto–Charon system can be found elsewhere (cf. Stern 1992; Stern *et al.* 1997).

The importance of the Pluto–Charon system goes well beyond its stature as the last of the known planets. The Pluto–Charon system also constitutes the two largest known objects in the Kuiper Belt, and is the best known example of a binary planet. Further, Pluto itself is thought to display highly-dynamic volatile transport, and is one of the three members of the fascinating Titan–Triton–Pluto triad of cryogenic, hydrocarbon-rich worlds in the outer solar system.

Because Pluto is a planet with so many interesting at-

 0004-6256/97/113(2)/827/17/$10.00

TABLE 1. Summary of observations.

#	JD (exposure mid-time)	UT Date	File ID	Exp(s)	Fil 1	Fil 2	Fil 3	Fil 4	ϕ	λ	r	Δ	α
0*°	2449524.07327	1994/06/20 13:45:31	x2bq0101t	1505		F275W	F1ND	F278M	12.8	22.6	29.784	28.954	1.14
1	2449524.12794	1994/06/20 15:04:14	x2bq0103t	688		F275W	F1ND	F278M	12.8	19.6	29.784	28.955	1.14
2*	2449524.13997	1994/06/20 15:21:33	x2bq0104t	613	F4ND			F410M	12.8	18.9	29.784	28.955	1.15
3	2449524.14977	1994/06/20 15:35:40	x2bq0105t	350	F4ND			F410M	12.8	18.3	29.784	28.955	1.15
4*°	2449524.20838	1994/06/20 17:00:04	x2bq0106t	1665	F4ND			F410M	12.8	15.0	29.784	28.956	1.15
5*°	2449525.61548	1994/06/22 02:46:17	x2bq0301t	1535		F275W	F1ND	F278M	12.8	295.7	29.785	28.969	1.18
6	2449525.66944	1994/06/22 04:04:00	x2bq0303t	658		F275W	F1ND	F278M	12.8	292.7	29.785	28.969	1.18
7*°	2449525.68146	1994/06/22 04:21:18	x2bq0304t	643	F4ND			F410M	12.8	292.0	29.785	28.969	1.18
8*	2449525.69145	1994/06/22 04:35:41	x2bq0305t	350	F4ND			F410M	12.8	291.4	29.785	28.969	1.18
9*°	2449525.74212	1994/06/22 05:48:39	x2bq0306t	1635	F4ND			F410M	12.8	288.6	29.785	28.970	1.18
10•	2449533.52690	1994/06/30 00:38:44	x2bq0201t	1535		F275W	F1ND	F278M	12.6	209.9	29.786	29.050	1.37
11	2449533.58016	1994/06/30 01:55:26	x2bq0203t	658		F275W	F1ND	F278M	12.6	206.9	29.786	29.050	1.37
12•	2449533.59218	1994/06/30 02:12:44	x2bq0204t	643	F4ND			F410M	12.6	206.2	29.786	29.050	1.37
13	2449533.60216	1994/06/30 02:27:07	x2bq0205t	350	F4ND			F410M	12.6	205.6	29.786	29.050	1.37
14•	2449533.65286	1994/06/30 03:40:07	x2bq0206t	1635	F4ND			F410M	12.6	202.8	29.786	29.051	1.37
15	2449535.13623	1994/07/01 15:16:10	x2bq0401t	1535		F275W	F1ND	F278M	12.6	119.2	29.786	29.068	1.40
16	2449535.18936	1994/07/01 16:32:41	x2bq0403t	658		F275W	F1ND	F278M	12.6	116.2	29.786	29.068	1.40
17•	2449535.20138	1994/07/01 16:49:59	x2bq0404t	643	F4ND			F410M	12.6	115.5	29.786	29.068	1.40
18	2449535.21136	1994/07/01 17:04:22	x2bq0405t	350	F4ND			F410M	12.6	114.9	29.786	29.069	1.40
19•	2449535.26205	1994/07/01 18:17:21	x2bq0406t	1635	F4ND			F410M	12.6	112.1	29.786	29.069	1.40

*Brief loss of guide star lock occurred during exposure.
°Day-to-night transition occurred just before exposure.
•Day-to-night transition occurred during exposure.

tributes, the quest to resolve its surface has been a long sought-after goal for planetary science. Unfortunately, the combination of Pluto's small size (diameter ~2300 km), and great heliocentric distance (presently just under 30 AU), conspire to result in an angular diameter of just ≈0.1 arcsec. As a result, no ground-based system has yet been able to resolve features on Pluto's surface.

In fact, the only surface "maps" of Pluto that have been obtained, were constructed by indirect light-curve inversion techniques. Several such inversion maps have been reported, including those of Marcialis (1983), Buie & Tholen (1989), Buie *et al.* (1992), Young & Binzel (1993), Reinsch *et al.* (1995), and Drish *et al.* (1995). The most common dataset used to generate such inversion maps are rotational light curves, however, mutual event light curves have also been employed to better constrain the Charon-facing hemisphere of Pluto. These various maps have revealed important details, but discrepancies between the maps limit their ultimate utility. A more detailed accounting of this work may be found in the recent reviews provided by Binzel & Hubbard (1997) and Buie *et al.* (1997b).

Resolved images of Pluto were first obtained by other groups using *HST* in 1990, 1991, and 1993, but the combination of *HST*'s initially poor (i.e., pre-COSTAR) imaging performance and the observing modes chosen to carry out these studies prevented many substantial details from being resolved on Pluto's surface (e.g., Albrecht *et al.* 1994).

The project described in this paper was proposed for *HST* in 1988, approved in 1989, and initially scheduled for execution during *HST* observation cycle 1, in 1991. However, shortly after the telescope was launched in 1990, it was discovered that *HST*'s primary mirror suffered from a spherical aberration which significantly compromised its imaging performance, particularly at subarcsecond scales. As a result, our project was delayed until after the imaging performance of *HST* was restored by the installation of COSTAR during the first *HST* Servicing Mission in 1993 December. The data we report on here were obtained in mid-1994, during cycle 4.

Our objective was to obtain the highest possible resolution on Pluto that *HST* presently allows. By using the Faint Object Camera (FOC) in its highest resolution mode, and by observing Pluto at blue and ultraviolet wavelengths where the Rayleigh resolution limit is most favorable, we estimated that 4 to 5 resolution elements could be placed across Pluto's diameter, and therefore, that a global Mercator projection map with ≈40–55 independent resolution elements could be achieved. This resolution offered the opportunity to resolve the major albedo provinces on the planet, and discriminate between the various indirect-mapping solutions obtained from light-curve and mutual event photometry. Additionally, by obtaining images on either side of the well-established, ~3000–3700 Å absorption edge of refractory materials which acts as a discriminator between contaminated and pure ice regions (e.g., Wagner *et al.* 1987), we also planned to obtain information on the purity of the surface ices as a function of their location, a wholly new kind of input to volatile transport models. This report details the results of this project.

2. THE OBSERVATIONS

We planned the cycle 4 *HST*/FOC observations as follows. The FOC was configured in 512×512 pixel imaging mode, which combined with the FOC's 0.014 arcsec pixels, resulted in a 7×7 arcsec field of view (FOV). This FOV is much larger than both the ≈1 arcsec scale of the Pluto–Charon binary, and the statistical uncertainty of *HST*'s blind pointing capability. As a result, we elected to image Pluto using blind pointing, which increased the efficiency of our limited, 8-orbit observation program. We specified that *HST* perform the Pluto imaging in Fine Lock Mode, which constrains the nominal image jitter to <0.005 arcsec; this is more than 20 times smaller than Pluto's diameter, and is almost an order of magnitude smaller than the *HST*+FOC point spread function (PSF).

Images of the Pluto–Charon system were obtained at four epochs during 1994 June 20 to July 01. The four epochs were chosen to image Pluto at four specified sub-Earth longitudes approximately 90° apart. As a result, complete (though sparsely sampled) rotational coverage was obtained.

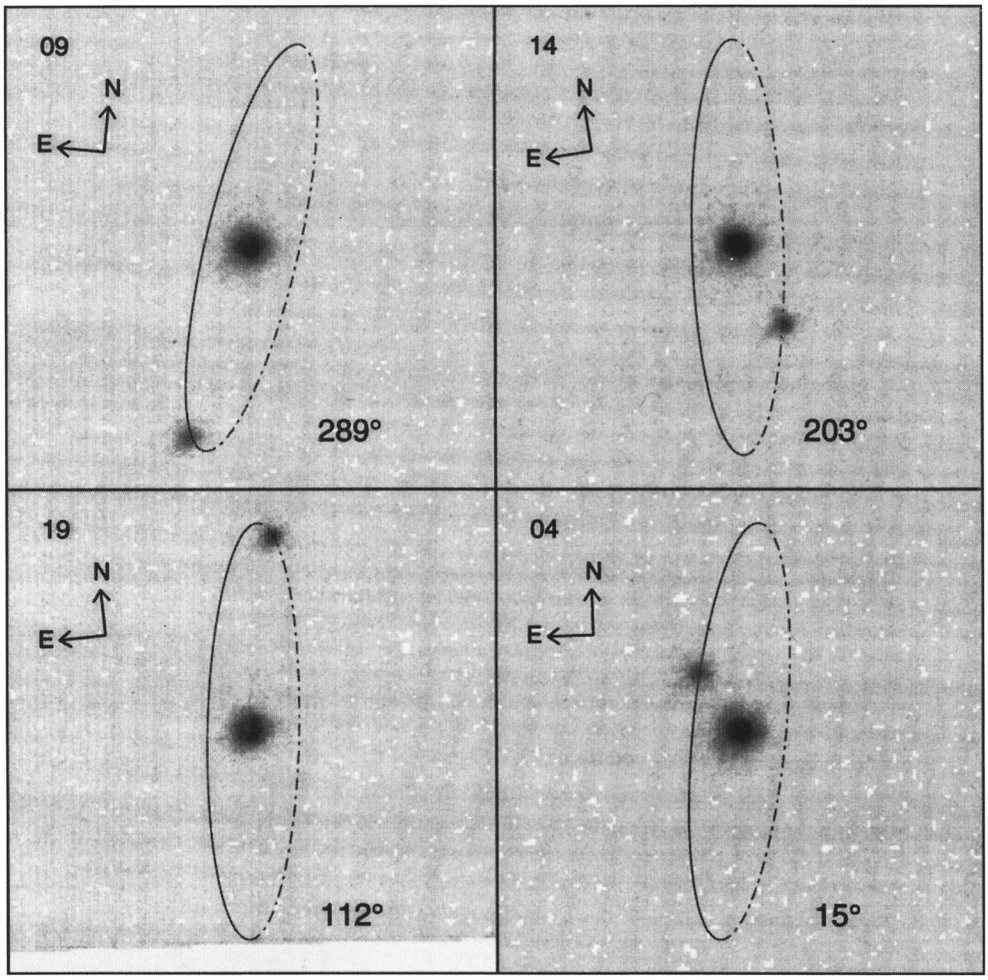

FIG. 1. The geometry and scale of the Pluto–Charon system as seen on the sky at each of the four FOC imaging epochs. Our image identification number for each panel (cf. Table 1) appears in the upper left corner of the panel; the number in the lower right corner of each image is the light-time corrected sub-Earth longitude of Pluto at the exposure midpoint. Also shown are arrows indicating the direction of north and east on the plane of the sky. Pluto's north pole is to the right for this plane-of-sky orientation. Superimposed on the four FOC image is the projected orbit path of Charon computed from the known orbit, nominal FOC plate scale, and the image orientation. The solid portion of the orbit path is the half that comes out of the plane of the picture. Note the excellent agreement between the expected positions and the actual radial locations of Charon in each image.

We constrained *HST* to obtain the four imaging epochs within a narrow time window (i.e., <3 Pluto rotations) in order to ensure a common observing geometry, a narrow range of solar phase angles, and little chance for secular changes due to possible, small-scale volatile transport.

At each imaging epoch, *HST* obtained 5 FOC frames of the Pluto–Charon System over a period of about 3 hr. During this time, Pluto turned through only 2% of a rotation, or about 7° in longitude (equator turns ≈145 km). This degree of movement is small compared to *HST*'s best possible resolution element scale of about 25° of longitude (450 km) at the equator. Table 1 summarizes the log of the 20 *HST* images we obtained for this program, as well as the geometric and Plutocentric circumstances of each image. Also included there for reference is a short image identification number (first column) that will be used throughout this paper.

The five images we obtained at each rotational epoch were partitioned into a visible (VIS) and an ultraviolet (UV) group. The VIS group at each epoch consisted of two long (i.e., ~1600 s) and one shorter (i.e., ~500 s) image made using an in-series combination of the FOC's F410M bandpass and F4ND neutral density filters. The neutral density filter was required to keep the FOC's count rate within its linear regime. The UV group consisted of one long (i.e., ~1500 s) and one short (i.e., ~700 s) mid-UV exposure made using an in-series combination of the FOC's F278M, F275W, and F1ND filters. Again the neutral density filter was used to keep the FOC's count rate within its linear regime. The F275W filter also served as a wide-band blocking filter against red leaks; the combination of UV filters F278M and F275W assured an out-of-band red leak of $<10^{-6}$.

Figure 1 illustrates the observing geometry of the system during the observations we conducted. This figure depicts the orientation of Pluto and Charon as seen on the sky at the midpoint of each of the four rotational epochs when images were obtained. Owing to Pluto's high (≈120°) obliquity, Pluto's angular-momentum (i.e., right-hand rule) north pole lies at a position angle near 270°. In what follows, all references to Pluto north will refer to this direction.

All 20 of the FOC Pluto images were processed by the *HST*/STSDAS pipeline FOC reduction software. These reductions included the removal of instrument bias, dark

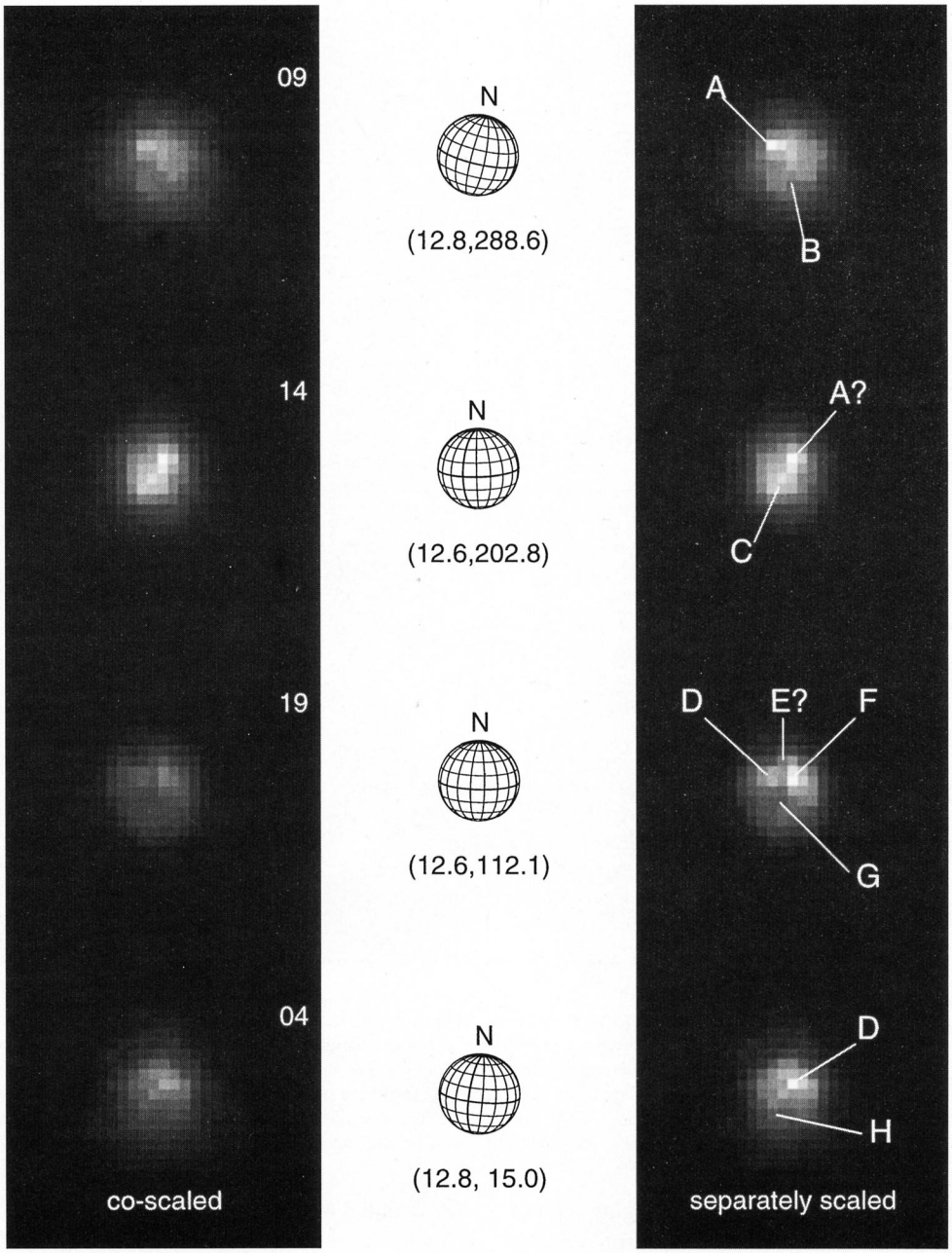

FIG. 2. These are our best signal-to-noise images in visible light (F410M) at each rotational epoch. Pluto's angular momentum north pole is oriented upward in all images; Pluto's morning limb is to the left. The left column of images are scaled to preserve the relative intensity between all four frames. The right column scales each image individually to show the maximum structural detail. The center column shows a wire-frame grid scaled to the apparent size and geometry of Pluto for each image. The latitude and longitude indicated below each wire-frame is the east longitude for the sub-Earth point at the time of mid-exposure in each image. The letters A through H in the right-hand column label prominent features detected repeatedly in the VIS images. Note that some features are even detected in more than one image set as Pluto rotates (e.g., D). Rotation advances from the top frame to the bottom frame. Image identification numbers are shown on the left.

counts, bad pixels, geometric distortion, flat-field variations, and other image artifacts. Typical images contained about 60 FOC pixels on Pluto (the FOC oversamples the *HST* PSF). The F410M images obtained peak-pixel count rates of 0.12–0.17 counts/s on Pluto; F278M images obtained counts rates in the peak pixel of 0.025–0.042 counts/s on Pluto. The count rate variations between images obtained in a given filter result from a combination of Pluto's large rotational lightcurve modulation, slightly changing geometric circumstances, flat-field effects, and counting statistics; Pluto's rotational modulation greatly dominated these variations. All 20 FOC images are shown in Appendix A.

3. IMAGE PRESENTATION AND INITIAL ANALYSES

In what follows we adopt some important definitions. We define an *image* as any depiction of Pluto projected onto the sky as a disk. We define a *map* as a derivative projection of Pluto images unwrapped onto a Mercator format. We further distinguish between *data images*, which are FOC products, and *rendered images*, which are produced from maps, for comparison to data images.

Figure 2 shows the best (i.e., longest exposure) VIS pipeline processed images at each of the four rotational phases at which we obtained data. In the left-hand column, these four

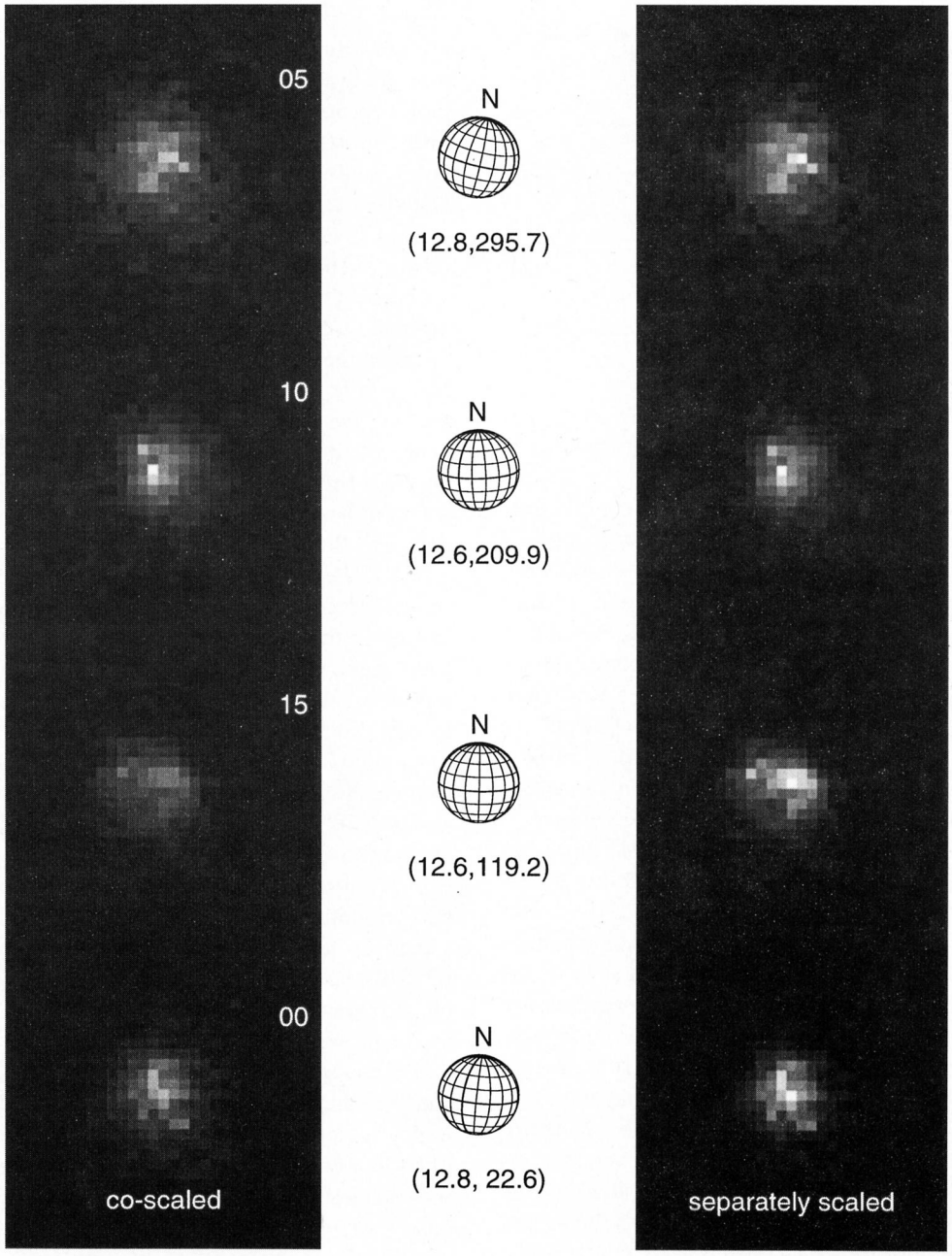

FIG. 3. These are our best signal-to-noise images in the UV band (F287M+F275W) at each rotational epoch. As in Fig. 2, Pluto's angular momentum north pole is up in all images, and rotation advances from the top frame to the bottom frame. The left column scales the images to preserve the relative intensity between frames. The right column scales each image individually to show the maximum detail. The center column shows a wire-frame globe drawn at the actual scale and orientation of Pluto in each image, and the image's sub-Earth latitude and longitude at the time of mid-exposure in each image. Image identification numbers are shown on the left.

images of Pluto were scaled as a group to reveal Pluto's distinct light curve. In the right-hand column each image was scaled individually to its own brightest pixel, in order to bring out surface details. The center column of Fig. 2 depicts geometric information. Figure 3 is similar to Fig. 2, but depicts the best UV image and the geometrical information relevant to each rotational epoch.

In Sec. 5, we will make comparisons of these images (and maps created from them) to Pluto's B and UV light curves, and to synthetic maps created from the inversion of light-curve and mutual event photometry.

Inspection of the full set of VIS and UV images in our FOC dataset (cf., Appendix A) reveals strong similarities between the three VIS images at each rotational epoch; a similar correspondence occurs between the two UV images taken at each rotational epoch. Most differences between exposures in a given filter at the same rotational epoch can be attributed simply to differences in counting statistics.

We now briefly discuss the main features of the VIS and UV images which are shown in Figs. 2 and 3. A primary criterion for the identification of surface features in the FOC images is the requirement we imposed for a feature's repeatability in all images made at a given rotational epoch and

TABLE 2. Summary of surface markings.

Ftr	Type	(ϕ,λ)	Reflectivity
A	bright	(+30°,255°)	0.87
B	dark	(−30°,220°)	0.49
C	bright	(−5° ,190°)	0.93
D	bright	(+30°, 70°)	0.77
E	dark	(+50°,110°)	0.54
F	bright	(+30°,175°)	0.83
G	dark	(+0° ,120°)	0.17
H	dark	(−10°,320°)	0.27

filter bandpass.[1] Such features are identified in Fig. 2 by letters. Short descriptions of the detected features can also be found in Table 2.

• *Sub-Earth Longitude 289° VIS Image (09):* At this rotational epoch, the most prominent feature is a northern bright spot near the morning limb (feature A). In the southern hemisphere we also identify a dark region (feature B), which trends diagonally across the image from near-equatorial latitudes at the morning limb to nearly polar latitudes near the evening limb. *UV Image (05):* In the F275W+F278M bandpass, Pluto appears quite different. There is no evidence for feature A, and only weak evidence for feature B. However, the high noise level of this UV image is reason to caution against overinterpretation of these apparent differences.

• *Sub-Earth Longitude 203° VIS Image (14):* Pluto has turned 86°. The planet presents itself near lightcurve maximum, and clearly displays bright features in both the northern and southern hemispheres. Feature A appears to have rotated across the meridian and now appears near the evening limb of the northern hemisphere. However, because the bright feature labeled A in image No. 14 does not noticeably appear in both of the other two long F410M images made near this sub-Earth longitude, we cannot say with certitude it has been detected at this rotational epoch, and therefore label it with a question mark. In the south, a new, prominent bright unit (feature C) has become visible to the morning side of the central meridian. Feature C is the largest bright province at this rotational epoch, and contains the brightest confirmed F410M pixel on the planet at any rotational epoch.[2] (See Appendix A for a comparison of all images.) *UV Image (10):* Little structure is visible in the F275W+F278M bandpass, but the bright feature, C, is clearly identified in the UV.

• *Sub-Earth Longitude 112° VIS Image (19):* Pluto has turned 91°. This rotational epoch is near light curve minimum, but still displays evidence for an extensive, bright northern polar region which stretches downward toward latitudes near ~30° north. The north polar region very clearly appears to be asymmetric, with its morning quadrant (feature D) appearing smaller and less extended toward the equator than its evening quadrant (feature F). Additionally, the region appears bisected near the sub-Earth meridian by a dark lineation (feature E) which is closely aligned to Pluto's north-south axis. We caution, however, that unlike features D and F, feature E is not clearly detected in the other F410M images at this rotational epoch; as a result we consider the reality of this feature to be uncertain.

Turning to the southern hemisphere, we observe some evidence for a marginally enhanced reflectivity unit (feature G) near the central meridian at a latitude near −30°. *UV Image (15):* Though noisier due to reduced signal levels in the UV, the F275W+F278M images again reveal the prominence of the northern polar region, and the same east-west northern hemisphere asymmetry as in the F410M image. The southern hemisphere appears to show a distinctly UV-bright unit near Pluto's evening limb.

• *Sub-Earth Longitude 015° VIS Image (04):* Pluto has turned 97°. Feature D, which is detected in all three VIS images at this rotational epoch (as well as all three VIS images at longitude 112°), has rotated from about 45° to the morning side of the central meridian to approximately 45° toward the evening side of the central meridian, and appears to show evidence for a bright, narrow, crudely-linear extension (feature H) trending away from it toward the morning hemisphere in the south. The fact that this albedo feature emanates from a bright spot is intriguing, though neither its reality nor its geologic association with the bright spot cannot be confirmed. As at longitude 112°, the northern hemisphere is again predominant. *UV Image:* In the noisier F275W+F278M bandpass we detect little reliable structure, but do see some evidence for a UV-bright feature on the meridian which may be related to feature D.

Taken together, the FOC images of Pluto shown in Figs. 2 and 3 demonstrate that the planet's albedo pattern is quite highly variegated. Of the eight features (A through H) identified in the F410M images, all but E appear in the best two (i.e., longest exposure) F410M frames at each rotational epoch.

4. BLUE AND ULTRAVIOLET MAP CONSTRUCTION

To obtain additional information from the FOC images, we constructed a global reflectivity map. All previous attempts at Pluto map construction have been limited to inverting light-curve data, and have therefore been considerably more model-dependent than the inversion of direct images such as these.

We now describe the in-depth image analysis that we applied to the FOC data in order to extract VIS and UV maps which (i) remove various geometrical effects, including limb curvature foreshortening, and (ii) offer higher S/N by virtue of being image coadditions.

For each of the FOC frames, we fit a 41×41 pixel subsection of the frame, centered on Pluto. The sought after result was to find the best 8×8 grid of FOC-sized pixels (0.01435 arcsec/pixel; FOC Handbook, V5.0) centered on

[1]To consider any albedo feature at a given rotational epoch to be real, we required that it could be seen in all of the VIS images at that rotational epoch. We did not require that a feature be seen at more than one rotational epoch, because off-meridian foreshortening and phase-angle effects often make such identifications problematic in a dataset with sparse rotational coverage like this one.

[2]Feature "A?" appears to be brighter in this image than feature C. However, since Feature "A?" does not repeat in the other images, we have labeled feature C the brightest feature.

Pluto. The size of Pluto on this grid was computed from the known geometry (r, Δ), and an adopted surface radius of 1150 km. At the scale of these images, known errors in the surface radius of Pluto (cf., Tholen & Buie 1997) have little effect on our results. We chose not to fit for the size of Pluto, since it would be highly correlated with and biased by the choice of limb-darkening function. Pluto was, by definition, precisely centered in the 8×8 pixel grid. Although there are 64 tiles in the 8×8 Pluto grid, the four corner pixels never overlap the planet.[3] As such, we set the brightnesses of these four pixels identically equal to zero, and solved for the remaining 60 image tiles. The variables in the resulting model image were the (x,y) center of Pluto in the 41×41 grid, an average image background level, and the brightness of each of the 60 on-Pluto image tiles.

The steps in transforming from the fit to the observed image plane are: (i) multiplying each pixel in the fit grid by the area of overlap between the pixel and the disk of Pluto, (ii) inserting this area-weighted grid into the 41×41 array at the nearest integer pixel, (iii) convolving the 41×41 array with a suitable *HST*/FOC PSF, and (iv) performing a fractional pixel shift to precisely locate the center of Pluto.

4.1 Removal of the PSF

Before images can be transformed into a map, the effects of the point-spread function of the telescope and instrument must be removed. To remove the PSF, we solved for the image that, when convolved with the PSF, would best match the observed image. This technique is superior to image deconvolution because it is less sensitive to subtleties of the actual PSF. However, it is important to note that the map which results from this process is ultimately limited by our knowledge of the PSF and *HST*'s real-time jitter history.

We found that having an accurate representation of the PSF is critical to accurate map extractions. In particular, the locations and brightnesses of markings on Pluto can be changed by any incorrect asymmetry in the PSF. Any error in the asymmetry of the adopted PSF is likely to be small, but remains a potential source of systematic error.[4]

The choice of a PSF was relatively constrained because no high-quality PSF calibration image library is available. As a result, we were forced to use a numerical PSF to model the image. We experimented with a number of different PSFs prior to the final extraction. Each numerical PSF was computed from a program provided by the Space Telescope Science Institute (STScI), named TinyTim; we used version 4.0b. We modified the TinyTim PSF by blurring it with a nominal jitter function that matched the average blurring of Charon on images. Through experimentation we found that even a grossly incorrect PSF hardly changed the markings in Pluto's equatorial regions. However, the reflectivity of polar areas, which are always near the limb, are more sensitive to the PSF choice and could be significantly affected by the exact shape of the PSF. As a result, we believe the polar regions of our derived maps and the rendered images created from them are less reliable than are the equatorial regions of our maps.

In seeking the brightness of each of the 60 valid image tiles in the 8×8 grid, we minimized the χ^2 of the observed minus model image. To do so we chose to use the Powell minimization algorithm described in Sec. 10.5 of Press *et al.* (1988).

One additional constraint was required in fitting the image tiles. This constraint is due to the 8 limb pixels that have a very small (about 5%) fractional overlap with the disk of Pluto. The value of these pixels should carry very little weight in the final result, and would have, if there were an upper limit to the brightness in the map. Though our software properly deweighted these pixels by area, we found that these 8 pixels were being driven to very high nonphysical reflectance values which led them to have a much stronger effect on the resulting map than they should. Since we expect the values of these pixels should be of little importance, we placed an arbitrary constraint on the inversion that forced the brightness of these 8 pixels to be equal to the *mean* of the brightnesses of the other 52 pixels, thus reducing the number of free parameters by 8. As with the choice of PSF, we found that the high-confidence (e.g., equatorial regions) were not sensitive to this constraint, but low-confidence regions in the map (e.g., the polar regions) showed marked changes after implementing this constraint. Our arbitrary constraint may not be the best solution, but we consider the approach reasonable, because it sets the limb pixels to plausible values. More importantly, those 8 limb pixels no longer controlled the outcome of the final averaged map. Instead, constraints from overlapping images, where these areas were less foreshortened, dominated in the final average.

4.2 Conversion from Fitted Image to Map

The reconstructed image at each rotational aspect was next transformed to a rectangular grid map. Limb-darkening and phase-angle effects were neglected.[5] The ORIENTAT keyword from the image header determined in the data processing pipeline at STScI was used to provide the plane-of-sky orientation of the image. The position angle of the North pole of Pluto was interpolated from values provided by the JPL/NAIF utility program MICA, v1.0. The angular size of Pluto and the sub-Earth latitude and longitude were computed from the orbital and rotational elements given in Buie *et al.* (1992). These geometric quantities are the only ones required for resampling the reconstructed image onto a Pluto-centric latitude/longitude grid.

4.3 Construction of Composite Mercator Maps

A composite, global map was constructed for both the VIS and UV datasets by a weighted average of their individual partial maps, with the weights set by the exposure times. Thus, the weight for the jth pixel in the ith map was set to $w_{ij} = \Delta t_i \mu_j \delta a_{ij}$, where Δt_i is the exposure time for the

[3]These are the corner pixels resulting from inscribing a circle within a square grid.

[4]We verified that this is a small error by a trial run with the PSF orientation orthogonal to the correct orientation.

[5]Buie *et al.* (1997b) have analyzed Pluto's limb darkening and found that a <10% effect occurs in the 150 km nearest the limb at blue wavelengths.

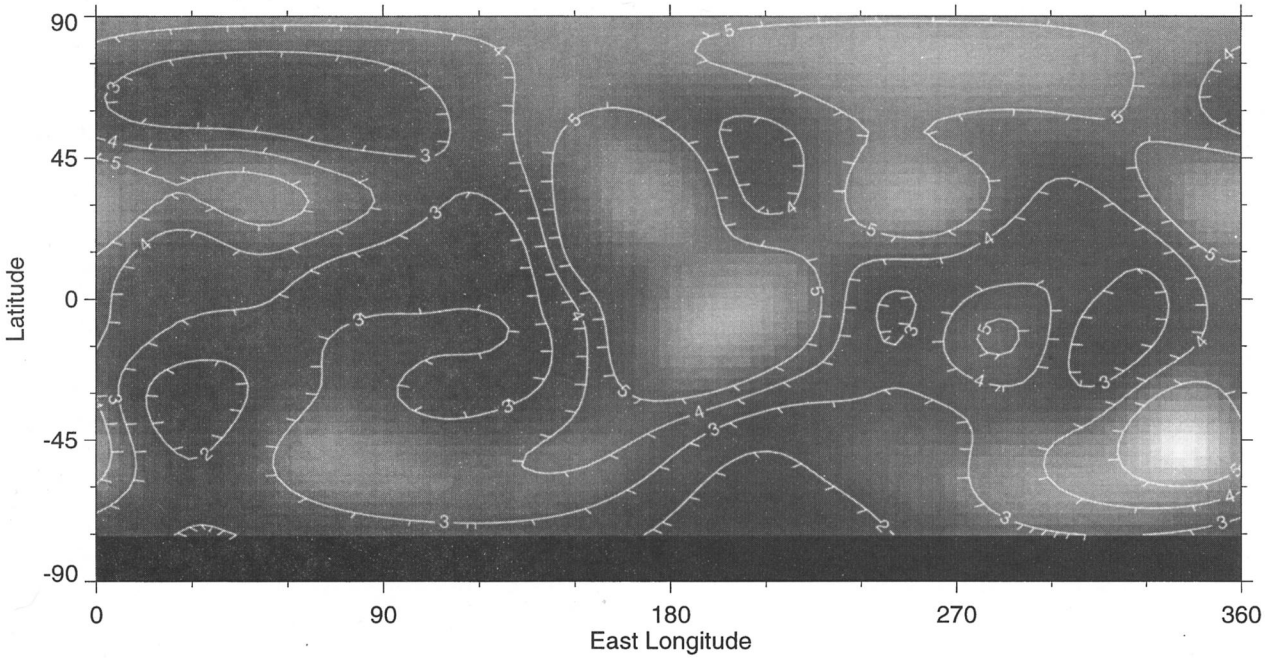

FIG. 4. This image shows a rectangular projection of the map of Pluto inferred from the F410M FOC ''VIS'' images. Overlain on the map are smoother significance contours of the reflectance value divided by its uncertainty (in units of standard deviation). These contours are computed on a per pixel basis. Higher numbers indicate areas of higher confidence. The tick marks indicate the ''downhill'' direction or direction to lower confidence. The black strip at the south pole is the area not seen by our images. As described in the text, the contrast in this map has been stretched from zero to the brightest pixel; we refer to this quantity in the text as ''relative reflectance.''

original image, μ_j is the cosine of the viewing angle relative to the surface normal (set to zero if the pixel is not visible), and δa is the fractional areal coverage on Pluto for the image pixel from which the ijth map element was determined. The weighted average gives more weight to both the longest exposures (highest signal-to-noise ratio), and to the FOC pixels near the center of the disk.

Because the flux integral over the partial maps was not as accurate as aperture photometry done from the original images, we re-scaled the partial maps to make their integral match the photometry. To ensure that no information was lost in the process of reprojecting and averaging the data, the working grid size for the maps was made considerably finer than the true resolution of the map. As a result, the raw weighted average image shows much more structure than is physically possible from the FOC images. Thus, the final step in the map construction was to smooth the global map to an appropriate spatial resolution. For this smoothing, we used a Gaussian filter with a 30° FWHM. This smoothing level ensures that structure at a scale finer than ≈600 km is not present in the final map. This smoothing was applied in a spherical coordinate system.

The final VIS and UV composite maps are shown in Fig. 4 (F410M) and Fig. 5 (F278M+275W). For the VIS map, we used 11 of the 12 VIS images.[6] For the UV maps, we used all eight available images; although a better product might be achievable by excluding one or more images from the final UV map construction, such a step would leave us with only one image at some rotational aspects, and would therefore make it impossible for us to compute statistical confidence measures (see next subsection).

Each map was stretched from zero to its maximum value for display. We call the resulting quantity, which is proportional to albedo, the ''relative reflectance.'' The overlain contours shown on these maps result from the error analysis discussed in the next subsection. The black strip at the south pole of each map is the portion of the surface not imaged by *HST* because of Pluto's northerly sub-Earth latitude.

Most of the features called out in Fig. 2 and Table 2 are present in Fig. 4. Feature A corresponds to the bright area near (+30, 255), where the number pair refers to (latitude, longitude) in degrees. Feature B is the somewhat dark area near (−30, 220). Feature C is the brightest spot in the map near (−5, 190). Features D and F correspond to the medium bright patches at (+30, 70) and (+30, 175). Feature E is related to the darker area near (+50, 110). Feature G is the darkest area in the map near (+0, 120). Feature H is the dark area near (−10, 320).

Detailed comparisons between the VIS images in Fig. 4 and the UV images in Fig. 5 will be made in Sec. 5, but we point out here that there is much similarity between the two maps, but there are also interesting differences. In particular, both the north and south polar regions appear darker in the UV than in the VIS map.

4.4 Error Analysis

It is critical to have an understanding of the significance of the detected features in the VIS and UV composite maps. A composite map was made from each set of four VIS or UV rotational epochs; in toto, 3 composite VIS maps and 2 com-

[6]We excluded image 04 because it created a significant discrepancy in the comparison of map derived to real light curves (see the final subsection of this paper). (Header records for image 04, we note, showed a pointing loss of lock during the exposure).

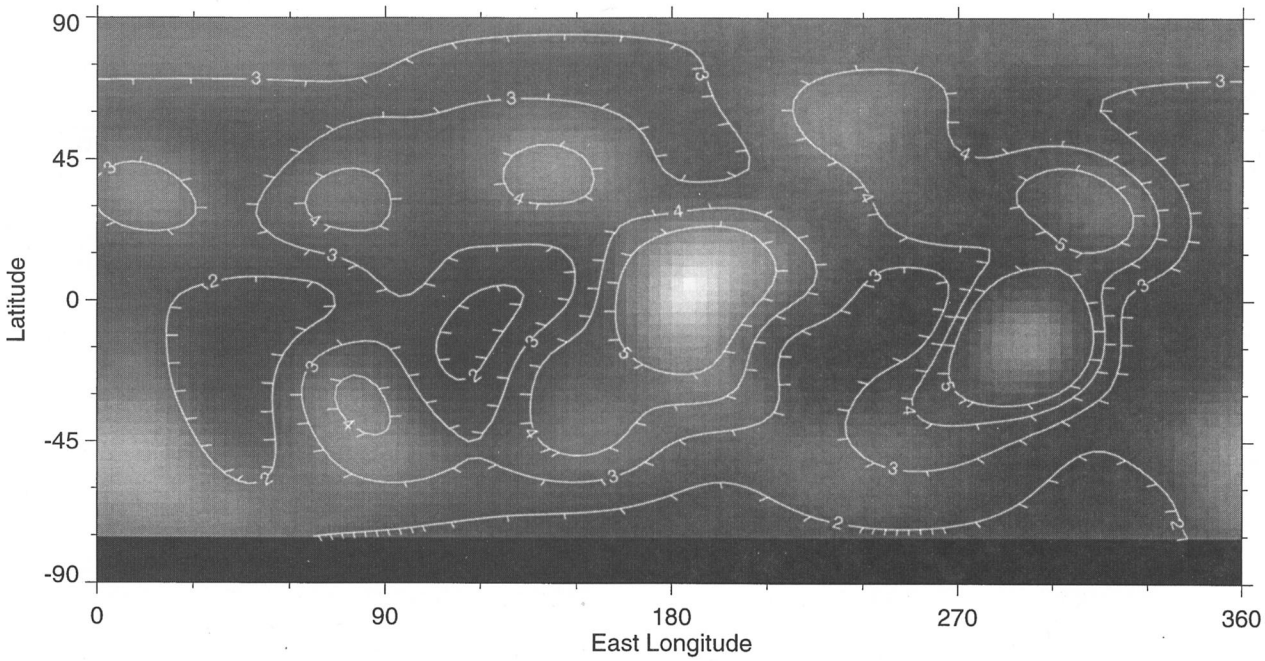

FIG. 5. This image shows a rectangular projection of the map of Pluto inferred from the F278M FOC ''UV'' images. Overlain on the map are smoother significance contours of the reflectance value divided by its uncertainty (in units of standard deviation). Higher numbers indicate areas of higher confidence. The tick marks indicate the ''downhill'' direction or direction to lower confidence. The black strip at the south pole is the area not seen in our images, due to Pluto's northerly sub-Earth latitude. As described in the text, the contrast in this map has been stretched from zero to the brightest pixel; we refer to this quantity in the text as ''relative reflectance.''

posite UV maps were made from the 20 FOC images we obtained. From the composite maps, an error (σ) image was derived, where $\sigma^2=\Sigma(m_i-\bar{m})^2/2$, m_i represents the individual composite maps, and $\bar{m}$ is the grand average map. For this step, we did not weight the individual composite maps for differing exposure times.

Because we only have three maps to input into the VIS error analysis and two maps to input into the UV error map, the derived uncertainties are not very well known on a point-by-point basis. After some empirical tests, we adopted a smoothing of the error image with a 25° FWHM spherical smoothing filter, which should be compared to 15° smoothing for the map. The smoothed sigma maps serve as a guide to general areas of good or poor consistency between the independently derived maps. The proper method of using these uncertainties is to compare the map values between two points separated by more than 600 km (the resolution of the map). If the two points differ by more than the stated uncertainties, then the two values are different. Comparisons between surface units closer than the resolution limit cannot be made since the values and their uncertainties will be correlated.

As stated above, the contours overlain on the maps in Figs. 4 and 5 are confidence levels in the map image. The confidence level results were derived by dividing the map by the error image ($\bar{m}/\sigma$). This overlay gives a general feel for how significant the given reflectance value is. As a result, our error map is a measure of the consistency between original images. Areas where the images do not agree lead to areas on the map that are more poorly known. High contours (i.e., $\sigma=5$) show regions of high confidence and low numbers ($\sigma\leqslant 2$) indicate poorly determined areas. For example, the bright area in Fig. 4 near +30° and 260° is in the location of feature ''A?'' on Fig. 2. The fact that image No. 14 shows a feature that did not repeat in other frames produced a lower confidence measure in this area. Likewise, feature ''E?'' (+50,110) in Fig. 2 corresponds to an area in the VIS map in Fig. 4 where a low confidence contour almost traces out the linear feature seen in the original image.

4.5 Comparison of Composite Maps to Original Images

In deriving the maps we generated a set of rendered (i.e., synthetic) images to judge how well each matches the original FOC image. Recall that we intentionally degraded these rendered images by applying a TinyTim PSF to them.

The comparison between the FOC images and the rendered images from our composite maps is shown in Fig. 6 for the VIS images, and in Fig. 7 for the UV images. In each figure, the left-hand column shows the best image from each longitude (cf. Figs. 2 and 3). The center column shows a rendered globe made from the global map at a very fine pixel scale.[7] The right-hand column shows the result of rebinning the rendered-globe images in the center column to match the pixel scale of the FOC, and then degrading the result by convolving it with the FOC PSF used to invert each image. In effect, although we did not include synthetic Poisson noise on these computed images, this process provides an end-to-end reverse inversion of the map back to rendered

[7]The reader should note that the bright pixels on the limb of each rendered globe in the middle column of Figs. 6 and 7 are an artifact of the projection process that can amplify the apparent reflectivity of edge-on pixels. Because these artifacts involve a very small area, they are naturally suppressed by the algorithm that transforms them to rendered images in the right-hand column.

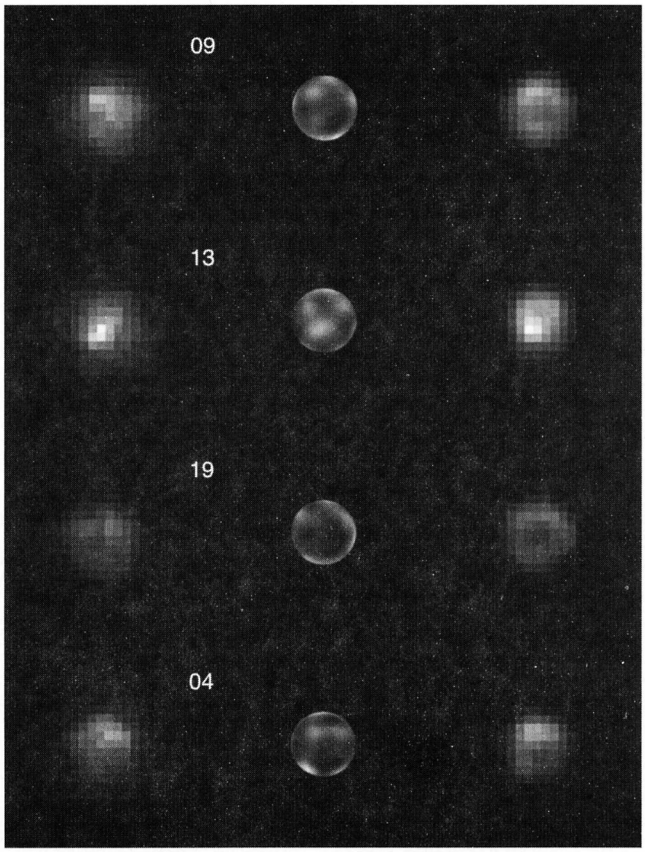

FIG. 6. Comparison of visible-band data and final map extraction. The images in each column have been co-scaled, so as to accurately depict relative brightnesses within a column. The left column shows the same images shown in Fig. 2 and their identification numbers. The center column is a high pixel-resolution VIS-globe image generated from the final, composite visible-band map. The right column is the result of degrading the images in the center column to FOC-sized pixels and convolving with the instrumental PSF. Pluto's north pole is again up in these images.

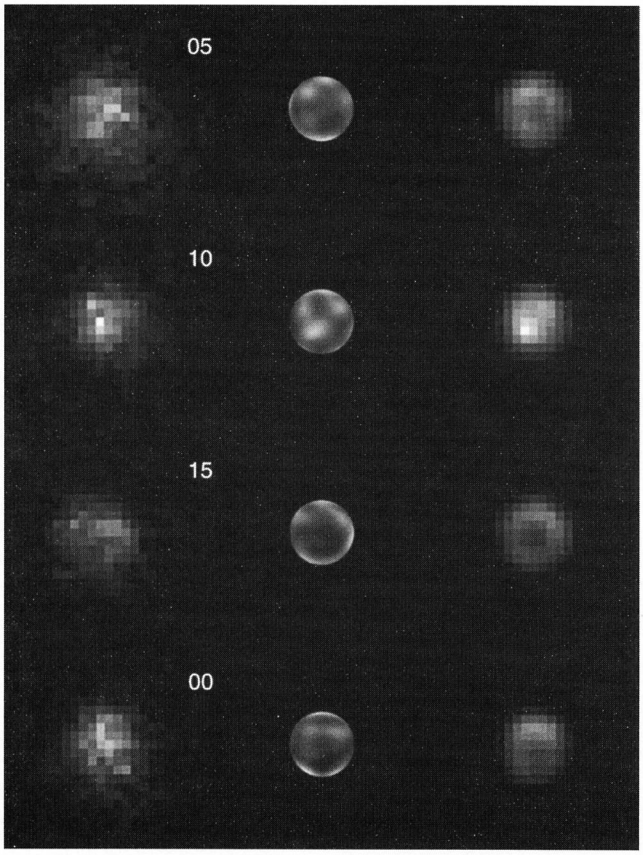

FIG. 7. Comparison of UV-band data and final map extraction. The images in each column have been co-scaled, so as to accurately depict relative brightnesses within a column. The left column shows the same images shown in Fig. 3 and their identification numbers. The center column is a high pixel-resolution UV-globe image generated from the final, composite UV-band map. The right column is the result of degrading the images in the center column to FOC-sized pixels and convolving with the instrumental PSF. Pluto's north pole is again up in these images.

images, so that they can be visually compared to the original data images. This result can be directly compared to the left-hand column to judge the quality of the map fit. Because the map algorithm does not guarantee a unique result, checks like these (and others described below) are required to ensure that the derived maps are valid. And indeed, the correspondence between computed and observed images is rather good. In fact, most differences between the two correspond to features that do not repeat between images made at the same rotational epoch, such as feature "A?" in the longitude 203° images and feature "E?" in the longitude 112° images.

4.6 Map Comparison to Light Curves

By their nature, the global maps we presented above predict a complete light curve for Pluto. We therefore generated synthetic light curves by computing hemispherical integrals for the VIS and UV maps as a function of longitude, which can be compared to an actual light curve of Pluto. The measured light curve we chose was obtained by another *HST* program in a bandpass centered at 4390 Å (Buie *et al.* 1997a), and transformed to Johnson *B*. This comparison is shown in Fig. 8, where we set the magnitude scale for Pluto's mean opposition distance (r=39.5 AU, Δ=38.5 AU).

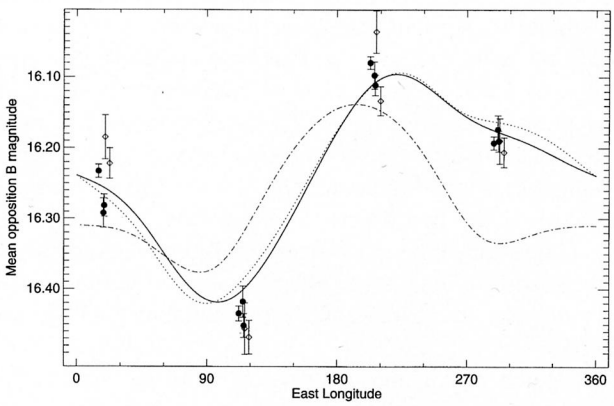

FIG. 8. Comparison of lightcurves inferred from the map to image photometry and to an independently derived, reference light curve. The solid curve is the Johnson *B* light curve of Pluto from Buie *et al.* (1997a). The dotted line is the light curve inferred from the visible-band global map in this work. The dot-dash line is the light curve inferred from the UV-band global map. The points with error bars are relative photometry derived from the FOC images. Filled circles are from the F410M images and the diamonds are from the F278M+F275W images. The inferred light curves and FOC photometry have been shifted so that the mean matches the midpoint of the known lightcurve.

The dotted line is the inferred light curve from the VIS map in Fig. 4; the dot-dash line is the inferred lightcurve from the UV map in Fig. 5; the solid line is the Buie *et al.* (1997a) *B* light curve. Since our images are not yet absolutely calibrated, we scaled the mean of the inferred light curves to match the mean of the observed *B* light curve.

Also plotted in Fig. 8 are relative photometric measurements of Pluto obtained from each of the actual FOC images. These points were derived by summing all the signal in each FOC image within a 10 pixel radius centered on Pluto (which itself had a radius of 4–5 pixels); such an aperture excludes Charon in every image. Within the calculated uncertainties, the direct photometry from the FOC VIS and UV images is consistent with the previously established (i.e., solid-line) light curve of Pluto. This tells us that the images themselves give a photometrically reliable lightcurve, and that the VIS and UV light curves are not dramatically different (at least at this sparse rotational sampling).

Now compare the two map-derived lightcurves to the "ground truth" (i.e., solid-line) light curve. The VIS map-derived light curve (dotted line) compares quite favorably. However, the UV map-derived light curve does not. This implies that the UV map is less reliable than the VIS map, which was expected, based on the lower S/N and small number of UV images. However, the poor correspondence of the UV light curve to the UV photometry also implies that our mapping algorithm has a deficiency. This deficiency may manifest itself in the UV as a result of the low S/N issue just noted, and we are investigating potential algorithm improvements. One possible improvement is that the algorithm may be improved with better jitter and PSF knowledge. In Sec. 6 we discuss this and other future map algorithm improvements we plan to undertake.

5. MAP INTERPRETATION

The VIS (F410M) map shown in Fig. 4 displays a bright northern polar region, a more variegated southern polar region, and a network of bright and dark features across the equatorial and mid-latitude regions of the planet. Notice that the cores of the distinct bright and dark units in this map are detected with confidence levels (i.e., S/N contours) exceeding 10 per pixel. We point out that the brightest region on the planet, which is centered near the equator and longitude 180°, corresponds to the longitude of Pluto's visible and UV light-curve maximum. We also point out that the most distinct dark equatorial region is located near 110° longitude, which closely corresponds to the longitude of Pluto's minimum light. Intriguingly, this dark region appears to be surrounded by a bright, but broken circular fringe.

The UV map shown in Fig. 5 has some strong similarities to the VIS map in Fig. 4. For example, in both the VIS and UV maps, the poles are on average brighter than the mid-latitude average (see also Fig. 14, which we discuss below). Also, the main equatorial dark spots seen in the VIS map, including the one near the sub-Charon point (i.e., 0° longitude), persist in the UV. Regions that are dark in both maps are likely to be particularly high in refractory materials. Prominent differences between the VIS and UV map are likely related to the level of ice contamination, and will be discussed in the next subsection. First, however, we wish to present a set of map-brightness histograms, and latitudinal and longitudinal averages.

Figure 9 (Plate 25) displays brightness histograms for the global VIS and UV maps, and histograms of three subset latitude bands for each. More specifically, the top panel shows the global map coverage fraction histogram as a function of VIS reflectance value (black), and histograms of the same quantity for the latitude bands +90° to +60°, +60° to +13°, and +13° to −30° latitude, which are depicted as red, green, and blue curves, respectively. The bottom panel is the same data product for the UV map.

In the global histograms, which are shown in bold in Fig. 9, one should notice that (i) both the VIS and UV show no significant features with relative reflectance <0.16 or >0.85, and (ii) each histogram peaks at a relative reflectance near 0.40–0.50. Despite these similarities, the shapes and peak amplitudes of the two histograms differ considerably. In particular, the VIS histogram shows a broader peak and a more symmetrical distribution on either side of the peak than does the F278M histogram. Although as we discussed above, the UV map is not as reliable as the VIS map, the UV histogram does appear to be substantially more asymmetric, and to display a steeper decline in the percentage of the surface brighter than the peak.

Now consider the three subhistograms shown for each map, showing the brightness distribution in different latitude bands. These subhistograms show that the darkest areas in each map are essentially confined to the equatorial zone, and that there is no other discrete range of brightness that is similarly confined in latitude. That is, bright- and intermediate-reflectivity terrain can be and is found everywhere, but the darkest material is only near the equator. It is also interesting to point out that the equatorial band has a bi-modal brightness distribution in the UV, and a highly skewed (almost flat) distribution in the VIS, suggesting the possibility of exposed, formerly ice-covered, involatile lag deposits. These findings are consistent with a net volatile transport from the equator to the poles in Pluto's current, near-equinox configuration.

These findings can be further amplified by inspection of Figs. 10 and 11, which show various cuts through the VIS and UV maps. To conserve space, we discuss only a few particularly noteworthy points about these figures. For example, we point out that in the cut made in panel A of Fig. 10 at longitude 200° (i.e., light curve maximum, panel A), the south pole is comparatively dark, but the equatorial and north polar regions are comparatively bright. Notice also that at longitude 92° (i.e., light curve minimum, panel C), both polar regions are bright, but the mid-latitudes are dark. Notice that the north pole is the brighter pole at longitude 92° cuts in both the VIS and UV. Also, the longitudinal cuts shown in panels B and D clearly show the influence of the bright features detected in the equatorial regions in images of the 180°–360° hemisphere. Finally, of note is the strong UV/VIS correspondence in the longitudinal map cuts. The fact that the UV and VIS are longitudinally similar but latitudinally different may indicate something about the role of

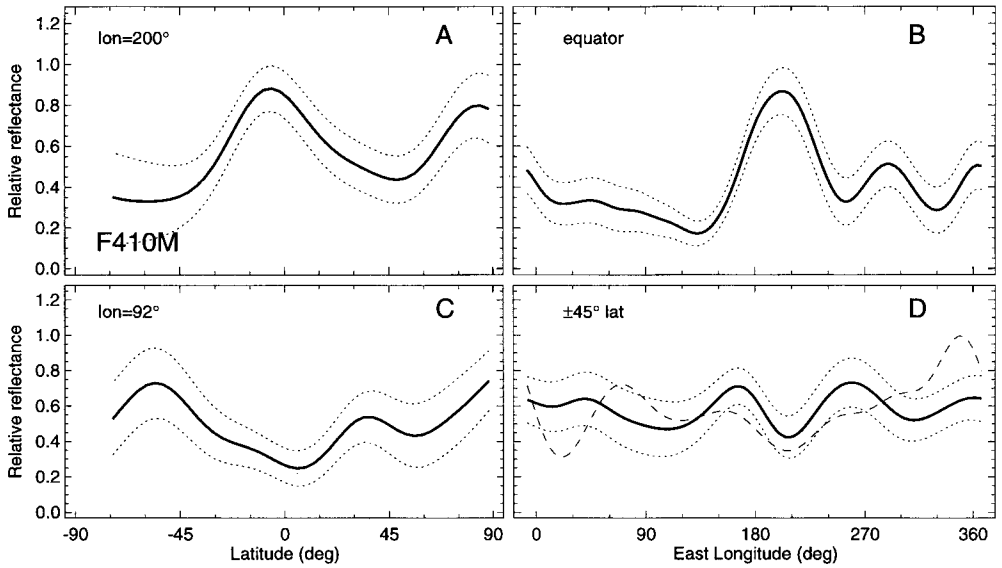

FIG. 10. Reflectance cuts through the composite VIS map of Pluto. These four panels (A–D) show various slices through the map shown in Fig. 4. In each plot the solid lines are the cuts across the map. Panel A is a cut from pole to pole at 200° longitude which corresponds to the longitude at maximum light in the light curve. Panel B is a cut through the map at Pluto's equator. Panel C is a cut from pole to pole at 92° longitude, which corresponds to the longitude of minimum light in the light curve. Panel D is a cut through the map at +45° latitude (solid line and 1σ bands) and at −45° (dashed line). The dotted lines show the smoothed 1σ error bands about the reflectance; these error envelopes are a direct measure of the statistical variance within each fixed-longitude band, as a function of longitude.

volatile transport or atmospheric contaminant deposition in generating the latitudinal distribution of albedos.

5.1 Compositional Information

As noted above, one rationale for our choice of both UV and VIS filters was to provide a compositional discriminator between surface units with clean ices, versus those units with ices contaminated by UV-absorbing materials.

Prominent mid-UV absorbers include organics (Thompson *et al.* 1987), sulfur compounds (Nash & Fanale 1977), NaCl and some sodium nitrates (Nash & Fanale 1977), and many (though not all) refractory minerals, including minerals frequently seen in meteorites and most lunar samples (cf. Wagner *et al.* 1987). The presence of such chemical compounds can be inferred by the presence of a commonly-displayed absorption edge between 3000 and 3700 Å.

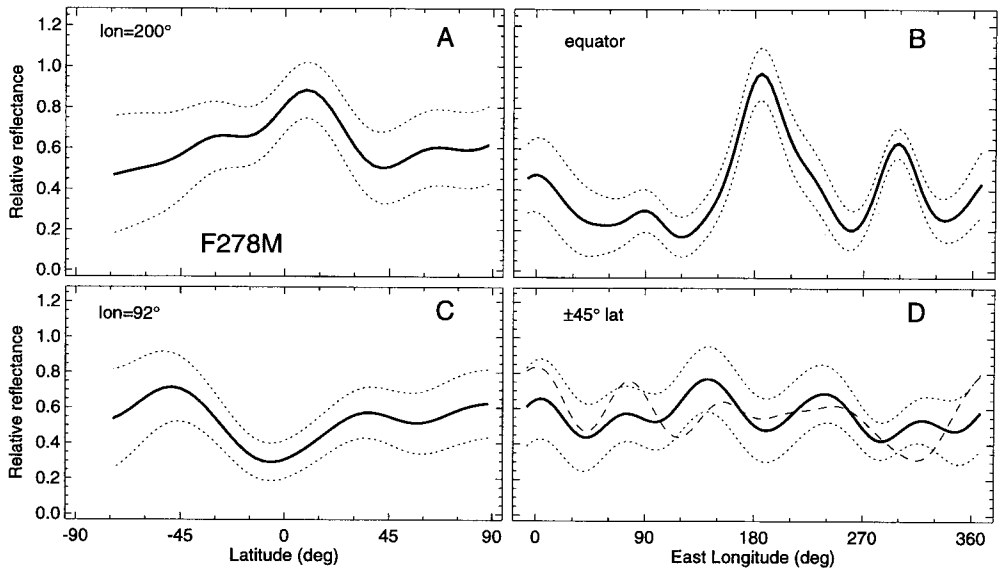

FIG. 11. Reflectance cuts through the UV map of Pluto. These four panels (A–D) show various slices through the map shown in Fig. 5. In each plot the solid lines are the cuts across the map. The dotted lines show the 1σ error bands about the reflectance. Panel A is a cut from pole to pole at 200° longitude which corresponds to the longitude at maximum light in the light curve. Panel B is a cut through the map at Pluto's equator. Panel C is a cut from pole to pole at 92° longitude, which corresponds to the longitude of minimum light in the light curve. Panel D is a cut through the map at +45° latitude (solid line and 1σ bands) and at −45° (dashed line). The dotted lines show the smoothed 1σ error bands about the reflectance; these error envelopes are a direct measure of the statistical variance within each fixed-longitude band, as a function of longitude.

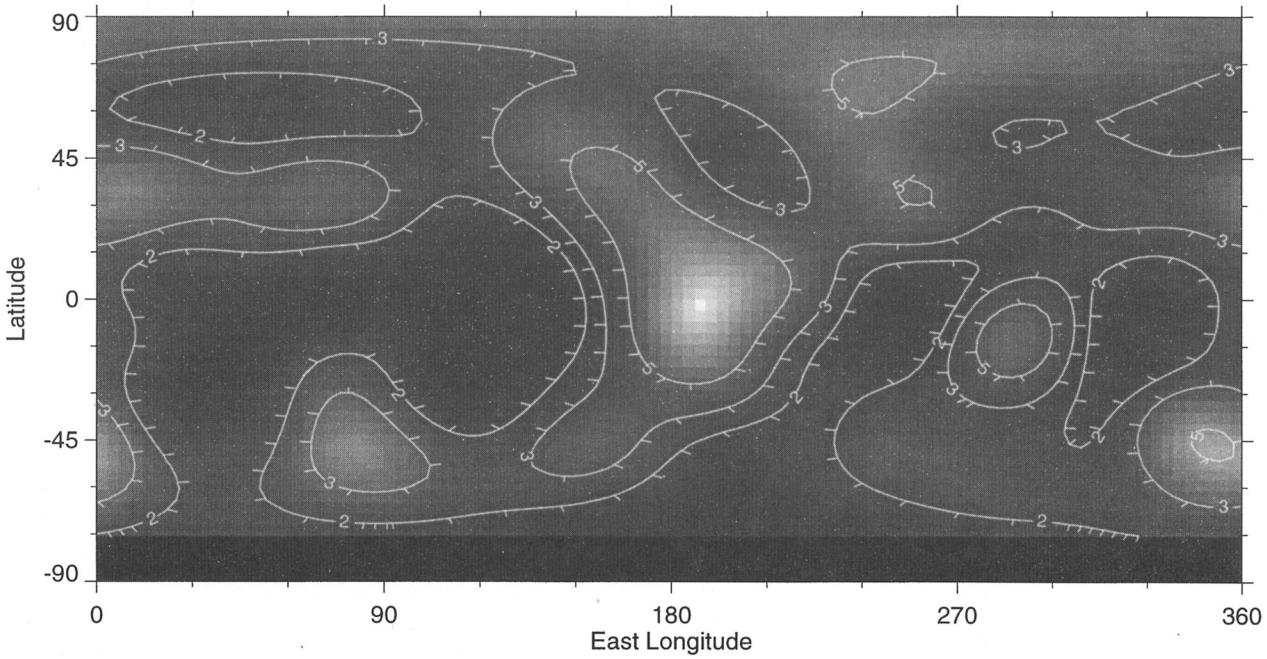

FIG. 12. Albedo product map of Pluto. This image shows a rectangular projection of the product of the visible and UV maps of Pluto, which is useful for estimating the purity of the surface ice (see text). Overlain on the map are significance contours of the reflectance product value divided by the uncertainty in units of standard deviation. Higher numbers indicate areas of higher confidence in the reflectance product. The tick marks indicate the "downhill" direction or direction to lower confidence.

In contrast, the frosts of H_2O, CO, CO_2, NH_3, CH_4, and N_2 are not strongly absorbing above 2500 Å (e.g., Lebofsky & Fegley 1976; Nash & Fanale 1977; Wagner *et al.* 1987), and have roughly-constant reflectance spectra between 2500 and 5000 Å. The spectral differences between these frosts and UV-absorbing materials can be used as a tool to discriminate between regions containing only relatively pure frosts, and those containing some degree of UV-absorbing materials, which might indicate either "bare ground," contaminated-frosts, or radiation-evolved frosts (e.g., Johnson 1989).

In Fig. 12 we make just such a comparison by showing the multiplicative product of the F410 and F275W+F278M maps. In such a product, brightness is proportional to the cleanliness of the ices. Thus, bright areas in Fig. 12 should correspond to clean ices and progressively darker areas should correspond to surfaces consisting of increasingly contaminated ices (or more purely refractory surfaces).

One striking aspect of the information presented in Fig. 12 is that the cleanest ice region on the planet apparently lies in the equatorial spot near longitude 180°, rather than at the poles. Equally striking is the fact that most of the darkest (and thus most contaminated) units preferentially lie in the equatorial belt. At this time it is not possible to determine whether the more contaminated regions are older (and thus more radiation darkened; Johnson 1989), or sites of preferential deposition of atmospheric photochemistry byproducts, or perhaps instead sites where more rapid sublimation revealed underlying lag deposits. The very dark regions in the VIS*UV product map spatially locate the UV absorbers previously inferred on Pluto through rotationally-resolved ultraviolet reflectance spectroscopy (Stern *et al.* 1991; Trafton & Stern 1996).

Figure 13 provides some additional insight into the clean ice versus refractory (or refractory-contaminated) surface units. This figure shows the longitudinally averaged relative reflectance from pole to pole for the VIS, UV, and VIS*UV maps. Such a curve is particularly useful for 1D volatile transport models, such as those recently presented by Hansen & Paige (1996). Notice that (i) the most contaminated ices are in the equatorial region, (ii) there are roughly symmetric "cleanliness" peaks some 40°–50° from the equator in each direction, and (iii) despite the fact that the cleanest unit in Fig. 12 is on the equator, the north pole is, on average, apparently the cleanest latitudinal zone seen on the planet.

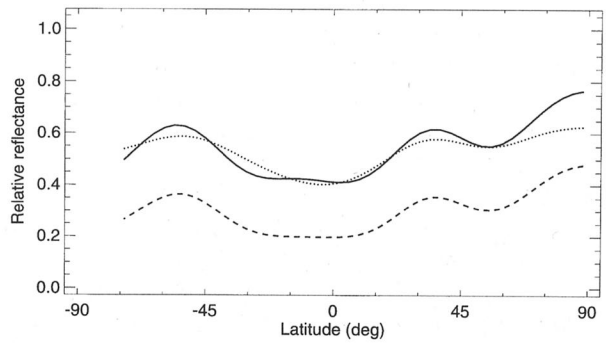

FIG. 13. These curves show a pole-to-pole plot of the longitudinally-averaged reflectance, as a function of latitude, for the VIS, UV, and VIS×UV maps shown in Figs. 4, 5, and 12, respectively. The solid curve is the visible reflectance; the dotted curve is the UV reflectance; the dashed curve below the VIS and UV curves is the UV*VIS reflectance product.

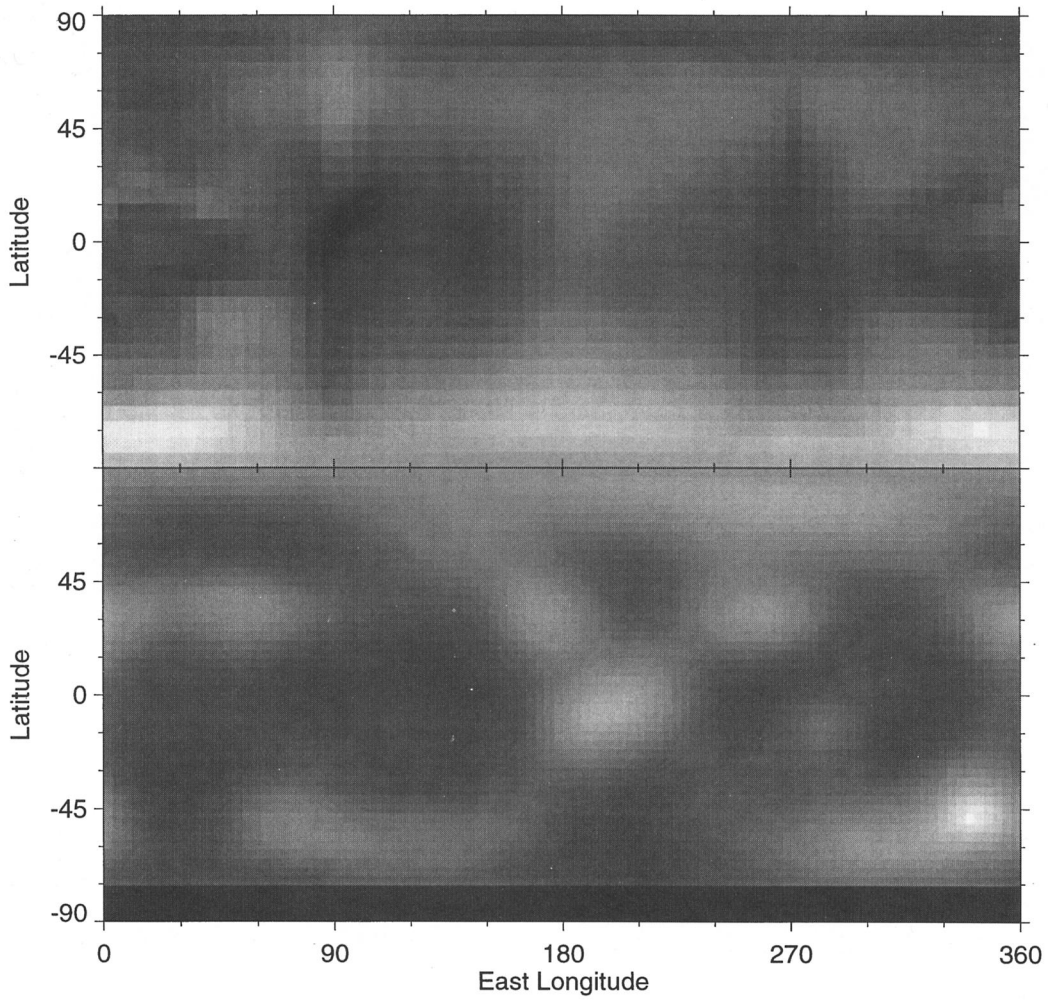

FIG. 14. MaxEnt lightcurve-inversion photometry and *HST* map comparison. The top map is the MaxEnt-derived map from Buie *et al.* (1992), converted to relative reflectance. The bottom map is the same as in Fig. 4, which is also in units of relative reflectance. Both maps have been stretched from zero to their brightest pixel.

5.2 Comparison to Previous Pluto Maps Constructed from Groundbased Rotational and Mutual Event Light Curves

In a future paper we plan to make a detailed comparison of the FOC maps to the various maps derived from mutual event and rotational light-curve photometry in order to evaluate the strengths and weaknesses of each Pluto map. For the present, however, we wish only to make some preliminary comments comparing our FOC-derived visible map with previously published, light-curve-inversion maps depicting the surface of Pluto. We focus here primarily on gross comparisons to the MaxEnt map (Buie *et al.* 1992). Although the MaxEnt map does not allow for temporal variations in Pluto's surface albedo pattern (Stern *et al.* 1988), whereas the more recent Drish *et al.* (1995) maps do, MaxEnt is the only global photometry map that is simultaneously constrained by both rotational lightcurves and mutual event photometry. It is also the map with which we are most familiar.

Figure 14 shows a direct comparison between the new VIS map and the older MaxEnt map. The effective (i.e., weighted-average) wavelengths of the two maps are quite similar. The MaxEnt map shown here has been converted from single-scattering albedo (as shown in Buie *et al.* 1992) to relative reflectance so that they can be easily compared to the maps derived from FOC data.

In the equatorial regions, there is a broad correspondence between the *HST*-derived and MaxEnt-derived maps. Having said this, however, there are also some notable discrepancies. The largest equatorial-region discrepancy comes in the longitude range of 90°–270°, where the MaxEnt map was constrained only by rotational lightcurves, without detailed knowledge of the light-curve contribution from Charon. If we treat the new, image-derived map as "truth," it appears that the MaxEnt map erred by putting a concentration of light centered on 180° at the south pole, whereas the *HST* shows the anti-Charon equatorial feature appearing much brighter. This is not particularly surprising, because little or no information is present for MaxEnt to accurately place features in the latitudinal direction in the anti-Charon hemisphere, where only rotational light curves are available. Another manifestation of this same limitation in the MaxEnt map are the "linear" north-south features it depicted at 90° and 270° longitude. Buie *et al.* (1992) attributed these fea-

tures to limb artifacts in the map extraction process since these locations are always seen on the limb during mutual events. By comparing the MaxEnt map to the *HST* map, it seems more appropriate to describe these "artifacts" as coming from a smearing of the true map features in the latitudinal direction by MaxEnt.

Turning now to the polar regions, we detect other differences between the *HST* and lightcurve inversion maps. In particular, the MaxEnt map implies that the south polar regions are brighter and more extensive than the north polar regions, which is opposite to what the *HST* images and the *HST*-derived maps show. Additionally, the relative reflectivity of the north polar region is quite different between the MaxEnt and FOC maps. Interestingly, although the map derived by Reinsch *et al.* (1995) predicts a dark north polar area which is even darker than in the MaxEnt map, the lightcurve-inversion maps produced by both Drish *et al.* (1995) and Young & Binzel (1993) predict a small and bright north polar cap that is in qualitative agreement with our FOC map.[8] If the north polar cap is indeed more extensive than the southern cap, as our images indicate, it would force a significant revision in thinking about volatile transport on Pluto (also, cf. Binzel 1990). Having said that, however, we must also say that we do not yet have enough confidence in the polar regions of our map to attempt to settle this discrepancy,[9] so we stress the fact that the equatorial regions are similar, and leave the issue of a polar discrepancy to a future paper.

6. SUMMARY AND CONCLUSIONS

We have obtained imaging coverage of Pluto using the Faint Object Camera (FOC) of the repaired *Hubble Space Telescope* (*HST*). This images constitute the first-ever longitudinally-complete direct imaging dataset on Pluto, and reveal more surface detail than had previously been available.

In toto, four sets of images were made at approximately 90° intervals in sub-Earth longitude during an 11-day period in mid-1994. Each of these four image sets consists of three F410M (≈410 nm, "VIS") FOC images and two F275W +F278M (≈278 nm, "UV") FOC images.

We have reduced all 20 of these images, and identified the prominent surface reflectance features on them. Based on these images, we report that Pluto's appearance is dominated by bright polar regions, and a darker but highly variegated equatorial zone which displays four bright subunits. The darkest unit on the equatorial zone appears to lie very close to the sub-Charon point, and appears to be ringed by a bright fringe. The two poles of Pluto are both bright, but they are not identical: the northern polar region appears to be both larger and brighter. Each of Pluto's bright polar regions appears to display a ragged border.

These *HST*/FOC images of Pluto's surface show a remarkable degree of variegation. In fact, although Iapetus displays a higher albedo contrast between its two major surface units, Pluto shows the largest number of distinct, high-contrast, large-scale albedo units in the outer solar system. Of particular note in this regard is the comparison of these *HST*/FOC Pluto images to recently-obtained *HST*/FOC Triton images (B.C. Flynn, PI; S.A. Stern, CoI), which reveal that Triton's surface shows dramatically less contrast and variegation than Pluto's.

From the FOC images, we derived complete maps of Pluto in the VIS and UV filter bands in which the planet was imaged. The derived maps can be improved, as evidenced by some discrepancies we have pointed out with respect to light-curve photometry and limb-darkening effects. Such work is now in progress. For the present, however, Fig. 15 (Plate 26) shows our existing VIS map, rendered to depict Pluto as a spherical globe.

By combining information from both the VIS and UV bandpasses, we were able to obtain information on the cleanliness of the frosts on Pluto, as a function of their location. Interestingly, the cleanest ice on the planet appears to lie at the equatorial bright spot near longitude 180°, which perhaps not coincidentally is near the anti-Charon point. Equally intriguing is the finding that the polar regions appear to be bordered by a darkish fringe. These images and maps will provide useful inputs to volatile transport models.

This paper constitutes the first report from our project to analyze these images. We plan to report additional details, after improving our mapping algorithm to include cross-image constraints, limb-darkening effects, and the small but nonzero contribution of Charon-scattered light. Additional improvements in the map of Pluto will also be possible by combining the *HST* images with groundbased photometry. We plan to report on the improved maps, and to make a thorough study comparing the *HST*-derived maps to the various photometry-inversion maps obtained by previous workers (e.g., Buie *et al.* 1992; Young & Binzel 1993; Reinsch *et al.* 1995; Drish *et al.* 1995).

We also plan to propose additional high-resolution imaging of Pluto in order to (i) obtain high-density rotational coverage to improve the quality of the maps; (ii) expand the wavelength coverage of the maps to provide both more compositional information and constraints on possible limb hazes, and (iii) search for temporal changes as Pluto draws away from perihelion.

Support for this work was provided by NASA through Grant No. GO.5330.01-93A from the Space Telescope Science Institute, which is operated by the Association of Universities for Research in Astronomy, Incorporated, under NASA Contract No. NAS5-26555. We thank our colleagues Brian Flynn for assistance with the initial visualizations of these data, John Spencer for extensive use of his workstation, and colleagues including Clark Chapman, Tony Reichhardt, and John Spencer for useful discussions. Rick Binzel, Walter

[8]The preferential agreement between the Young & Binzel map and our own, direct-imaging map, may be related to the fact that Young & Binzel's dataset included 1985 mutual event light curves that gave their dataset particularly good coverage of the north polar region of Pluto's Charon-facing hemisphere.

[9]Recall that in our treatment of the *HST* data, the polar regions (which always lie on the limb by their nature) are the most susceptible to systematic effects and cannot be trusted to the same level as the equatorial regions.

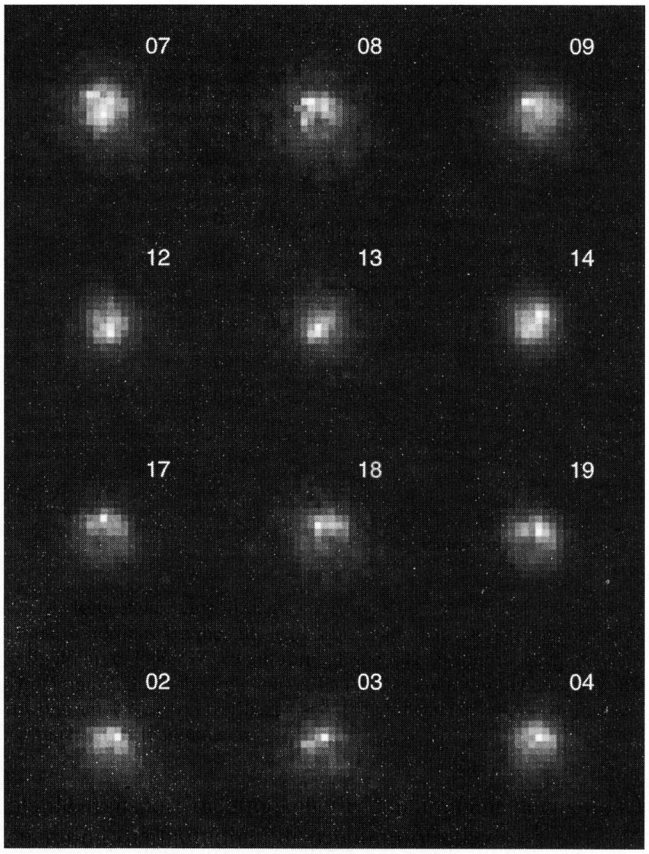

FIG. 16. The complete FOC VIS Pluto imaging dataset. These images are oriented with Pluto's angular momentum north at the top, and are shown with individual intensity scaling. The images are presented in the same longitude order as in Fig. 2. Each row in the image is at single imaging epoch, representing a similar sub-Earth longitude (cf. Table 1). Image identification numbers are to the upper right of each image.

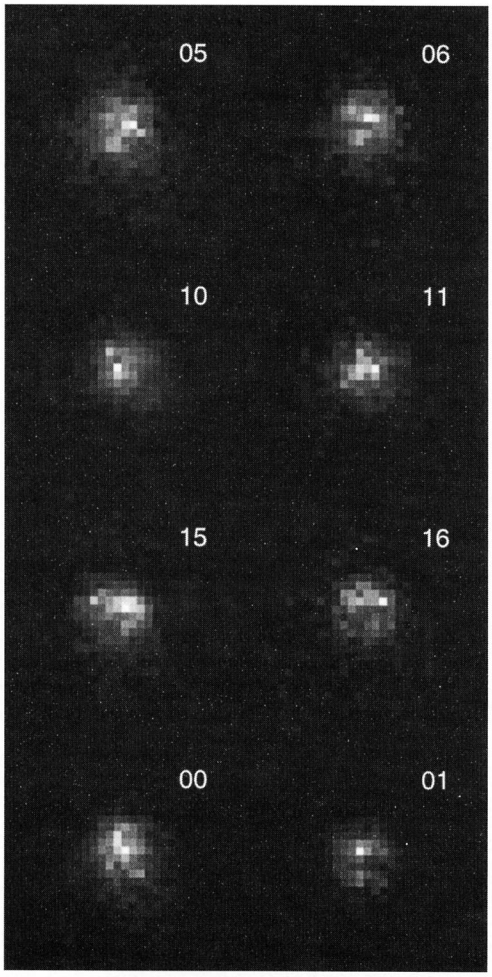

FIG. 17. The complete FOC UV Pluto imaging dataset. These images are oriented with Pluto's angular momentum north at the top, and are shown with individual intensity scaling. The images are presented in the same longitude order as in Fig. 3. Each row in the image is at single imaging epoch, representing a similar sub-Earth longitude (cf. Table 1). Image identification numbers are to the upper right of each image.

Wild, and an anonymous referee provided useful comments on this paper.

APPENDIX

Here, for completeness, we present the entire *HST* FOC Pluto dataset. Figure 16 contains all the FOC F410M (VIS) images; Fig. 17 contains all the FOC F278M+F275W (UV) images. The variation in signal-to-noise ratio between VIS images is particularly noticeable in Fig. 16 because the variation in exposure time is the greatest.

REFERENCES

Albrecht, R. *et al.* 1994, ApJ, 435, L75
Andersson, L. E., & Fix, J. D. 1973, Icarus, 20, 279
Andersson, L. E. 1978, BAAS, 10, 586 (Abstr.)
Binzel, R. P. 1989, GRL, 16, 1205
Binzel, R. P. 1990, LPSC, XXI, 87 (Abstr.)
Binzel, R. P., Tholen, D. J., Tedesco, E. F., Buratti, B. J., & Nelson, R. M. 1985, Sci, 228, 1193
Binzel, R. P., & Hubbard, W. B. 1997, in Pluto & Charon, edited by S. A. Stern, D. J. Tholen, and A. Schuman (University of Arizona Press, Tucson) (in press)
Buie, M. W., & Tholen, D. J. 1989, Icarus, 79, 23
Buie, M. W., Tholen, D. J., & Horne, K. 1992, Icarus, 97, 211
Buie, M. W., Tholen, D. J., & Wasserman, L. H. Icarus, 1997a (in press)
Buie, M. W., *et al.*, 1997b, in Pluto & Charon, edited by S. A. Stern, D. J. Tholen, and A. Schuman (University of Arizona Press, Tucson) (in press)
Christy, J. W., & Harrington, R. S. 1978, AJ, 83, 1005
Christy, J. W., & Harrington, R. S. 1980, Icarus, 44, 38
Cruikshank, D. P., Pilcher, C. B., & Morrison, D. 1976, Sci, 194, 835
Cohen, C. J., & Hubbard, E. C. 1965, AJ, 70, 10
Drish, Jr., W. F., Harmon, R., Marcialis, R. L., & Wild, W. J. 1995, Icarus, 113, 360
Elliot, J. L., Dunham, E. W., Bosh, A. S., Slivan, S. M., Young, L. A., & Wasserman, L. H. 1989, Icarus, 77, 148
Fix, J. D., Neff, J. S., & Kelsey, L. A. 1970, AJ, 75, 895
Hansen, C. J., & Paige, D. A. 1996, Icarus, 120, 247
Hoyt, W. G. 1980, Planets X and Pluto (University of Arizona Press, Tucson), p. 136
Johnson, R. E. 1989, GRL, 16, 1233
Lebofsky, L. A., & Fegley, M. B. 1976, Icarus, 28, 379
Marcialis, R. L. 1983, Master's thesis, Vanderbilt University, Nashville, TN
Nash, D. B., & Fanale, F. P. 1977, Icarus, 31, 40
Owen, T., *et al.* 1993, Sci, 261, 745

Press, W. H., Flannery, B. P., Teukolsky, S. A., & Vetterling, W. T. 1988, Numerical Recipes (Cambridge University Press, Cambridge)
Reinsch, K., Burwitz, V., & Festou, M. C. 1995, Icarus, 108, 209
Smith, B. A., *et al.* 1989, Sci, 246, 1422
Standish, E. M. 1996, in Completing the Inventory of the Solar System, PASP Conf. Ser. 107, edited by T. Rettig (in press)
Stern, S. A. 1992, ARA&A, 30, 185
Stern, S. A., Trafton, L. M., & Gladstone, G. R. 1988, Icarus, 75, 485
Stern, S. A., Tholen, D. J., & Schuman, A. 1997, Pluto & Charon (University of Arizona Press, Tucson) (in press)
Stern, S. A., Brosch, N., Barker, E. S., & Gladstone, G. R. 1991, Icarus, 92, 332
Tholen, D. J., & Buie, M. W. 1997, in Pluto & Charon, edited by S. A. Stern, D. J. Tholen, and A. Schuman (University of Arizona Press, Tucson) (in press)
Thompson, W. R., Murray, B. G. J. P. T., Khare, B. N., & Sagan, C. 1987, JGR, 92, 14933
Tombaugh, C. W., & Moore, P. 1980, Out of the Darkness: The Planet Pluto (Stackpole Books, Harrisburg), p. 218
Trafton, L. M., & Stern, S. A. 1996, AJ, 112, 1227
Wagner, J. K., Hapke, B. W., & Wells, E. 1987, Icarus, 69, 14
Walker, M. F., & Hardie, R. 1955, PASP, 67, 224
Williams, J. G., & Benson, G. S. 1971, AJ, 76, 167
Young, E. F., & Binzel, R. P. 1993, Icarus, 102, 134

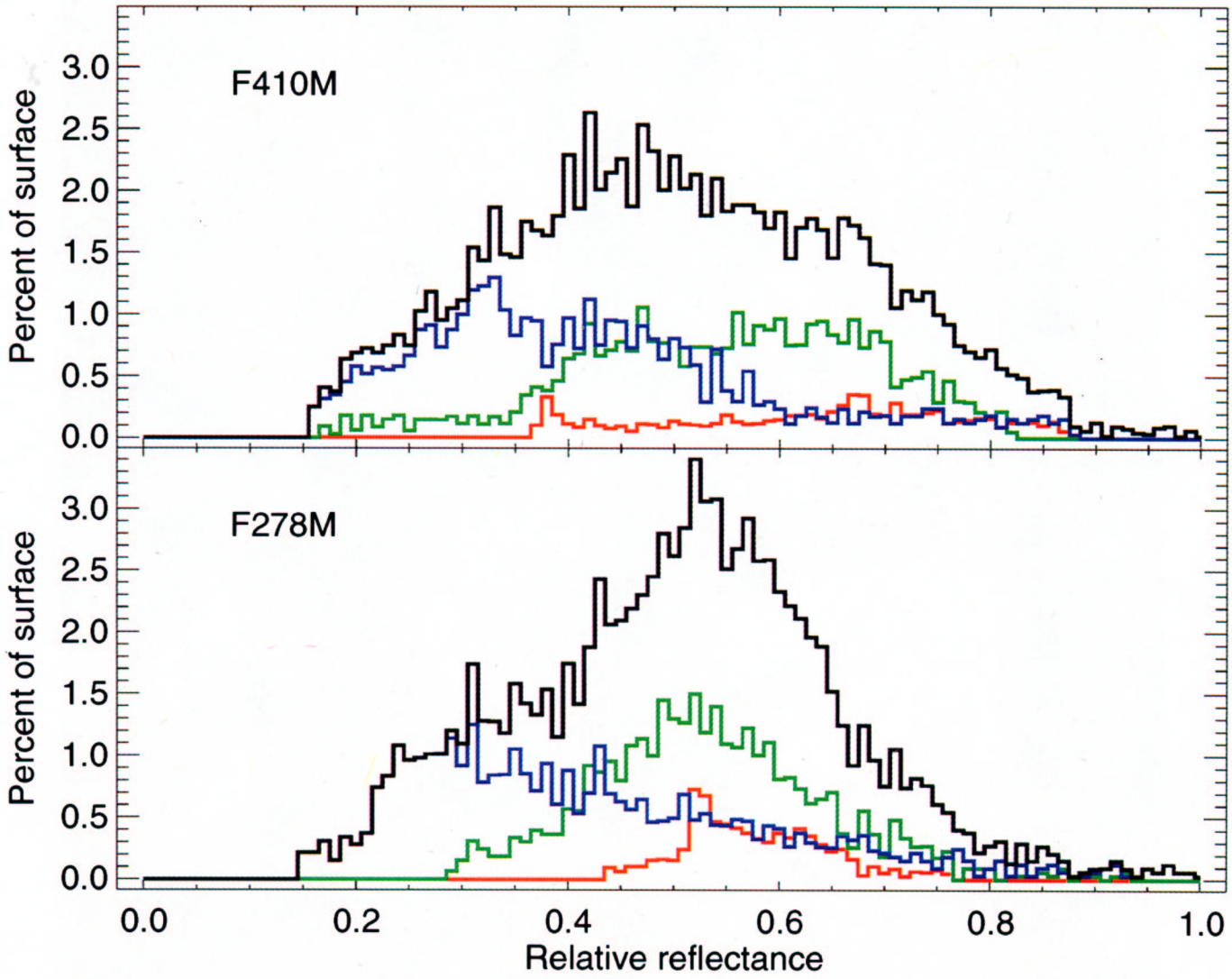

FIG. 9. Histograms of the UV- and VIS-band maps. The top panel shows a histogram of the surface coverage for the global visible reflectance (bold black), and subhistograms for three latitude bands: +90° to +60°, +60° to +13°, and +13° to −30° latitude, which are shown in red, green, and blue, respectively. The bottom panel is the same data product for the UV-band map. The unseen south polar region accounts for only 1.5% of the surface. The bin size in each histogram is in 0.01 of a relative reflectance unit.

Stern *et al.* (see page 837)

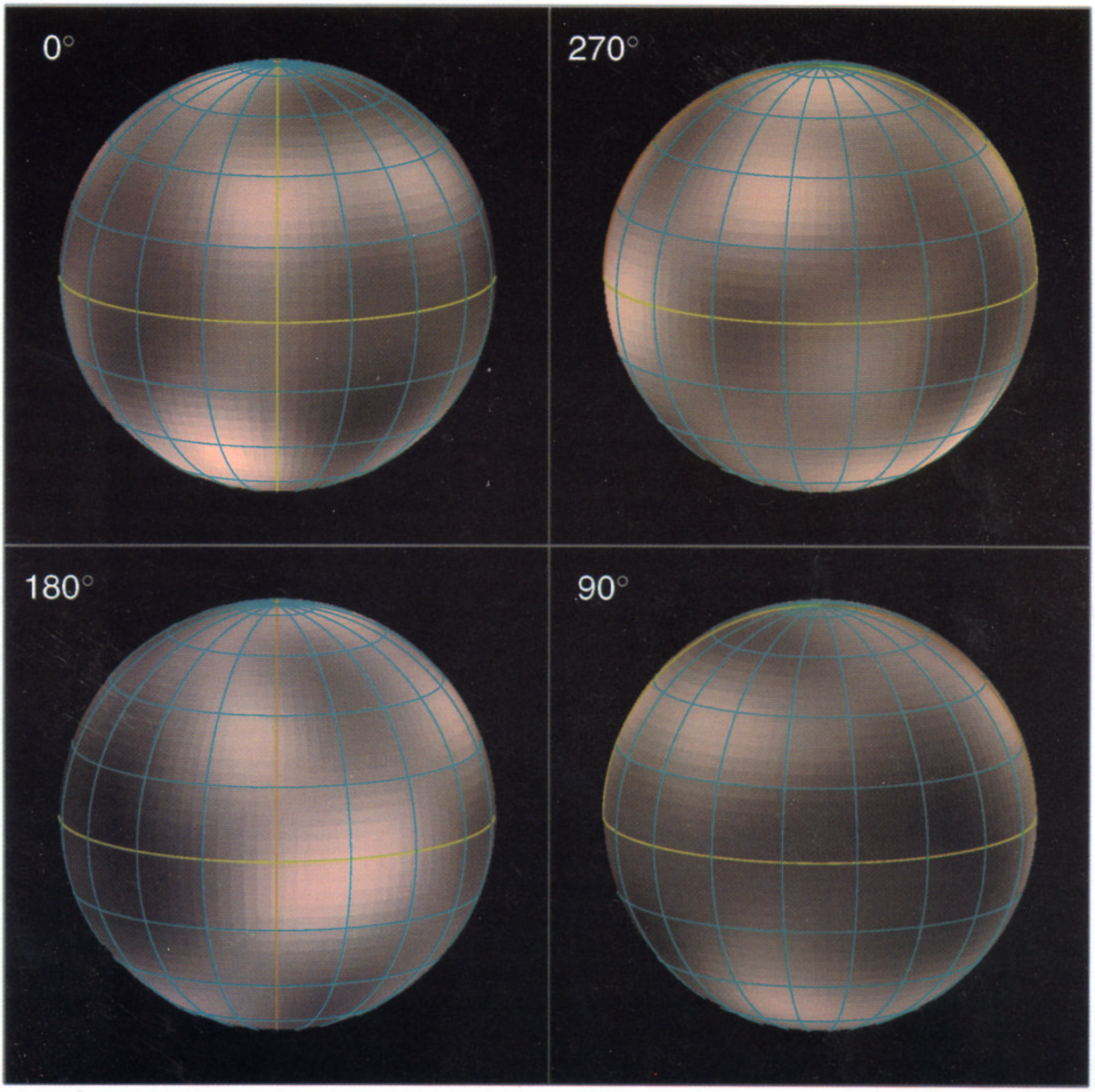

FIG. 15. *HST*-derived maps rendered onto three-dimensional globes at 90° increments in longitude. The rendered color was derived from the rotationally-averaged groundbased $B-V$ color of Pluto.

Stern *et al.* (see page 841)